Supporting Information

Highly Selective Photothermal CO_2 Hydrogenation to C_2^+ Hydrocarbons over Mn-Modified K-Fe Catalysts

Xinhuilan Wang[a], Alejandra Rendón-Patiño[a], Diego Mateo[a]*, Jorge Gascon[a]*

a Advanced Catalytic Materials (ACM), KAUST Catalysis Platform, King Abdullah University of Science and Technology (KAUST), Thuwal 23955-6900, Saudi Arabia

E-mail: diego.mateo@kaust.edu.sa; jorge.gascon@kaust.edu.sa

1. Catalyst Characterizations

Powder X-ray diffraction (PXRD) patterns were collected using a Bruker D8 Advance A25 diffractometer in Bragg-Brentano geometry with a Cu Kα source (λ = 1.54056 Å) operating at 40 kV and 40 mA. Data were acquired in continuous scanning mode over a 2θ range of 10° - 80° with a step size of 0.02° and a dwell time of 3 s per step. The PXRD patterns used in the quantitative phase analysis were acquired with a dwell time of 6 s per step. The crystalline phase was identified by comparison data from the inorganic crystal structure database, ICSD. Quantitative phase analysis was performed using the Rietveld method in GSAS-II.[1, 2]

Hydrogen temperature-programmed reduction (H_2-TPR) was conducted using a Micromeritics AutoChem II 2920 chemisorption analyzer. Prior to measurement, 100 mg of catalyst was pretreated under Ar flow at 150 °C for 60 min to remove surface-adsorbed species and subsequently cooled to 50 °C. The H_2-TPR profile was recorded by monitoring H_2 consumption as the sample was heated from 50 °C to 800 °C at a ramp rate of 10 °C min^{-1} under 10% H_2/Ar flow.

CO-temperature-programmed reduction (CO-TPR) was performed using the same instrument as for H_2-TPR. Firstly, the catalyst (200 mg) was pre-reduced in 10% H_2/Ar at 400 °C for 2 h, followed by cooling to 50 °C and helium purging for 30 min. The CO-TPR profile was recorded by monitoring CO consumption as the sample was heated from 50 °C to 800 °C at a ramp rate of 10 °C min^{-1} under 10% CO/He flow. Meanwhile, the CO consumption (m/z = 28) was monitored via mass spectrometry (MS).

CO_2-temperature-programmed desorption (CO_2-TPD) and CO-temperature-programmed desorption (CO-TPD) analyses were performed using the same instrument as for H_2-TPR. In each case, the catalyst (200 mg) was pre-reduced in 10% H_2/Ar at 400 °C for 2 h, followed by cooling to 50 °C and helium purging for 30 min. The sample was subsequently exposed to CO_2 or 10% CO/He flow for 60 min, followed by helium flushing to remove physisorbed species. The desorption profiles were recorded by heating the sample to 800 °C under helium flow at a rate of 10 °C min^{-1}. During this stage, a mass

spectrometer was used to monitor continuously the signals of the outlet gases, including CO_2 (m/z = 44), CO (m/z = 28), and H_2O (m/z = 18).

Elemental compositions, including Fe/Mn ratios and K content, were determined by X-ray fluorescence (XRF) spectroscopy using a HORIBA XGT-700 system.

N_2 adsorption-desorption measurements were performed using a Micromeritics ASAP 2040 instrument at 77 K. Prior to the analysis, the catalysts underwent a degassing process under vacuum at 150 °C for 720 minutes.

Photocurrent measurements were performed using an SP-150 potentiostat (Bio-Logic) electrochemical workstation with a three-electrode setup in 0.1 M Na_2SO_4 aqueous solution (pH = 7.0). The setup consisted of an FTO glass plate coated with the catalyst dispersion as the working electrode, a platinum foil as the counter electrode, and a saturated Ag/AgCl electrode as the reference. To prepare the working electrode, 400 µL of the catalyst dispersion (2 mg of catalyst mixed with 20 µL of 5 wt.% Nafion and 980 µL of ethanol) was drop-cast onto the FTO surface, covering an area of 1.0 × 1.0 cm^2.

The UV-Vis spectra were obtained by using a JASCO V-670 spectrophotometer. The diffuse reflectance spectra were obtained in a range of 250 - 800 nm using halogen and deuterium lamps as light sources

Transmission electron microscopy (TEM) was performed using a Titan ST microscope (FEI, Hillsboro, OR, USA) operated at 300 kV. Scanning transmission electron microscopy with high-angle annular dark-field imaging (STEM-HAADF) was conducted on a probe-corrected Titan MP microscope (FEI, Hillsboro, OR, USA) at the same accelerating voltage. The STEM-HAADF data were acquired with a convergence angle of 17 mrad and an inner collection angle of 49 mrad. Image acquisition and processing were carried out using *Velox* software. Elemental composition maps were obtained from energy-dispersive X-ray spectroscopy (EDXS) data, derived from background-corrected and fitted net intensities, and subsequently smoothed using a Gaussian filter ($\sigma = 0.7$). All samples were prepared in dry form and deposited on copper grids coated with ultrathin carbon films (300 mesh).

In situ diffuse reflectance infrared Fourier transform spectroscopy (*in situ* DRIFTS) measurements were performed on a Thermo Scientific Nicolet 6700 FT-IR spectrometer equipped with a Harrick Praying Mantis high-temperature reaction chamber. First, the pre-reduced sample was pretreated at 150 °C under N_2 flow for 60 min, and then the chamber was pressurized to 10 bar under N_2 at room temperature. Background spectra were recorded using 248 scans at a resolution of 4 min^{-1}. The reaction was initiated by introducing a 4:1 H_2/CO_2 mixture at 20 mL min^{-1}, with IR spectra collected every 2 min (128 scans per spectrum) over the 20-250 °C range (heating rate: 3 °C min^{-1}). To investigate the effect of illumination, a white LED source (UHP-T-WCS-DI, Prizmatrix) was introduced into the chamber during DRIFTS measurements.

^{57}Fe Mössbauer spectroscopy was performed at room temperature on the SEE Co W304 Mössbauer spectrometer. All samples were analyzed under ambient conditions. ^{57}Co(Rh) moving in a constant acceleration mode was used as the radioactive source, and spectral analysis was conducted assuming Lorentzian line shapes for computer-aided fitting.

Steady-state photoluminescence (PL) spectra were recorded in a Carry Eclipse Fluorescence Spectrometer using an excitation wavelength of 370 nm.

2. Supplementary Figures

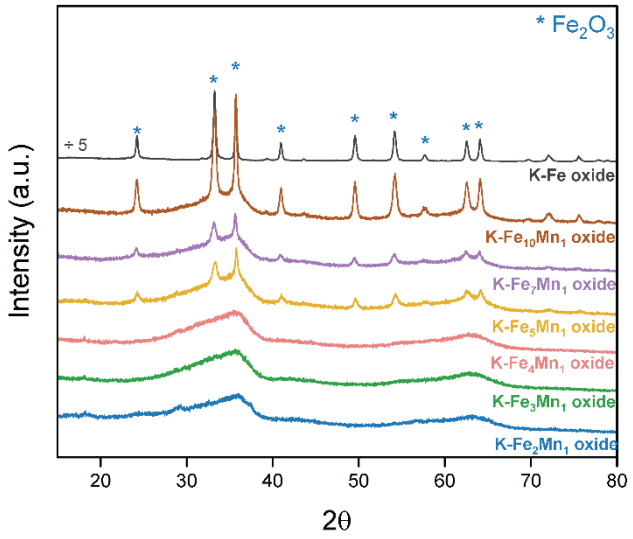

Figure S1. PXRD patterns for calcined K-Fe$_x$Mn$_y$/K-Fe samples.

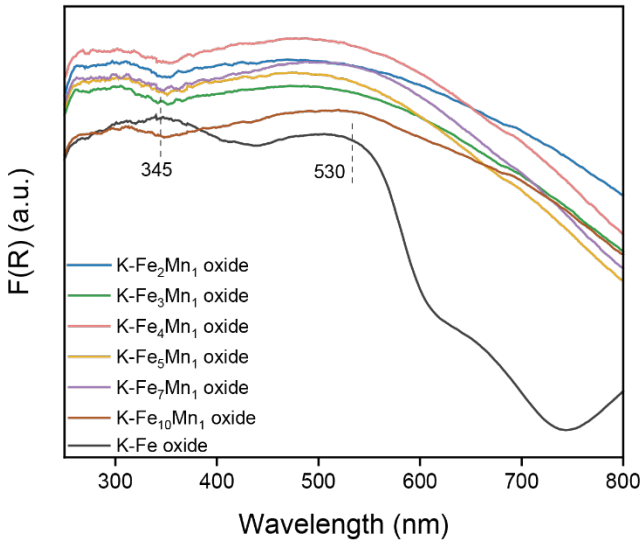

Figure S2. UV-vis-NIR absorption spectra of calcined K-Fe$_x$Mn$_y$ oxide.

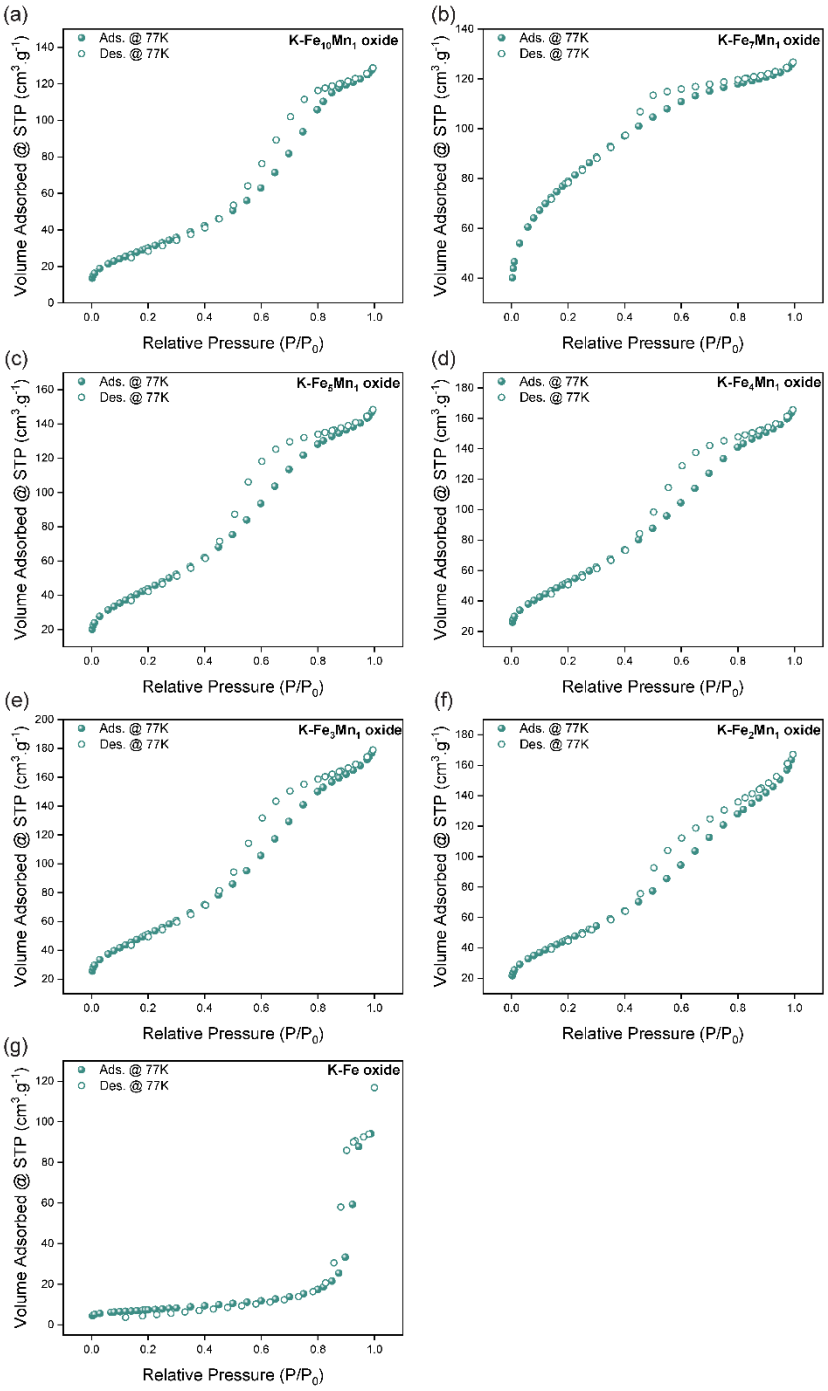

Figure S3. N_2 adsorption isotherms of K-Fe_xMn_y/K-Fe samples at 77 K.

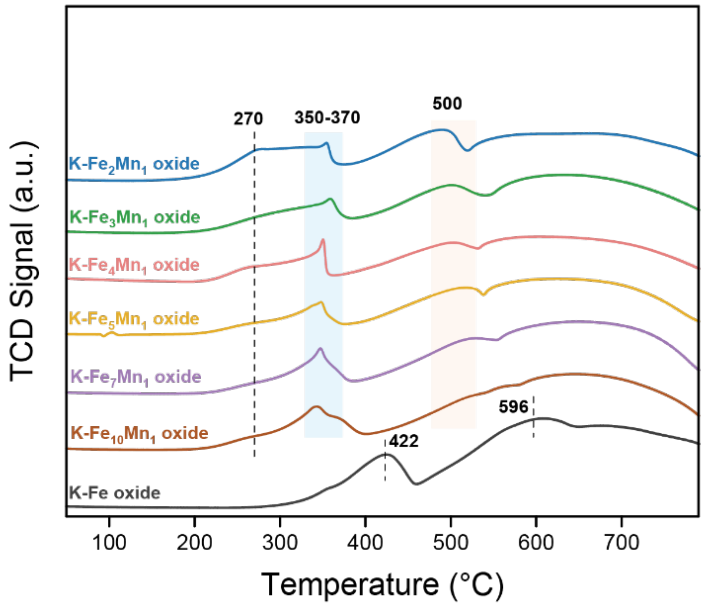

Figure S4. H_2-TPR for K-Fe_xMn_y/K-Fe samples.

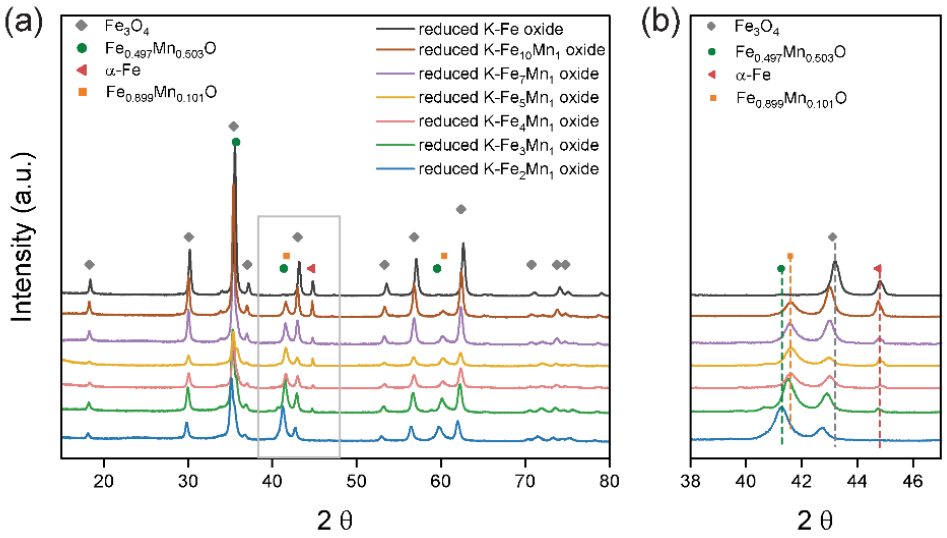

Figure S5. PXRD patterns for reduced K-Fe_xMn_y/K-Fe samples. Simulated XRD patterns for Fe_3O_4, $Fe_{0.497}Mn_{0.503}O$, $Fe_{0.899}Mn_{0.101}O$, and α-Fe are included.

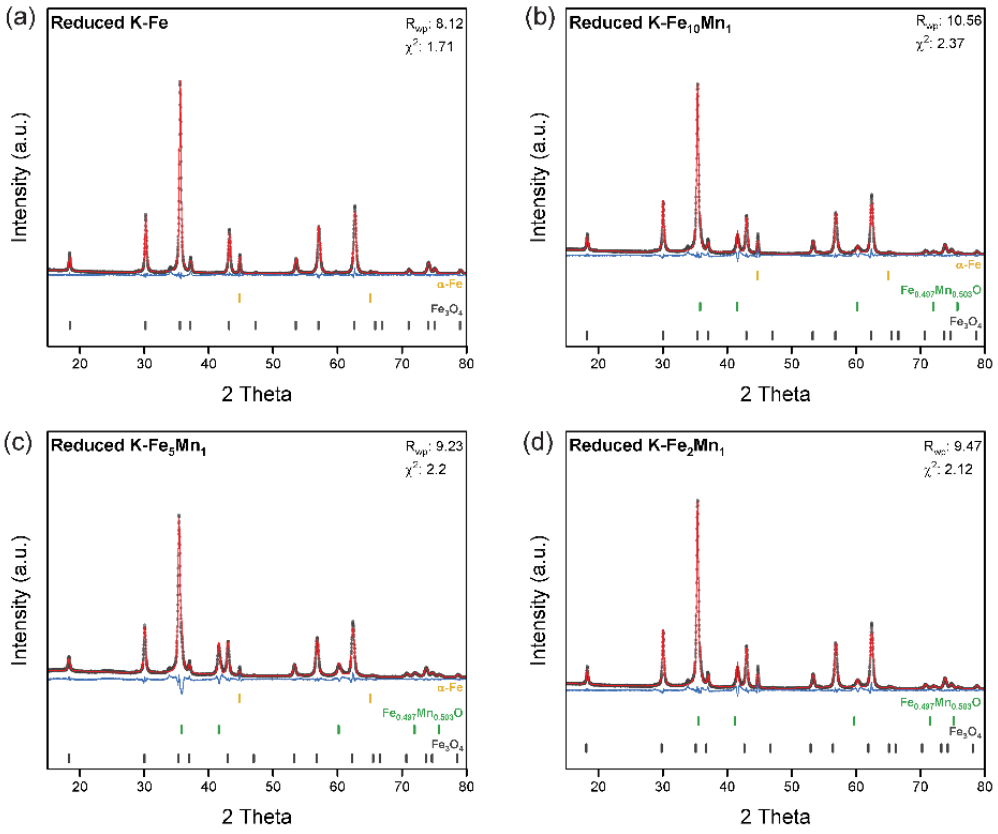

Figure S6. Rietveld plots showing obtained diffraction data, calculated intensities, and their difference for reduced catalysts (a) reduced K-Fe, (b) reduced K-$Fe_{10}Mn_1$, (c) reduced K-Fe_5Mn_1, and (d) reduced K-Fe_2Mn_1.

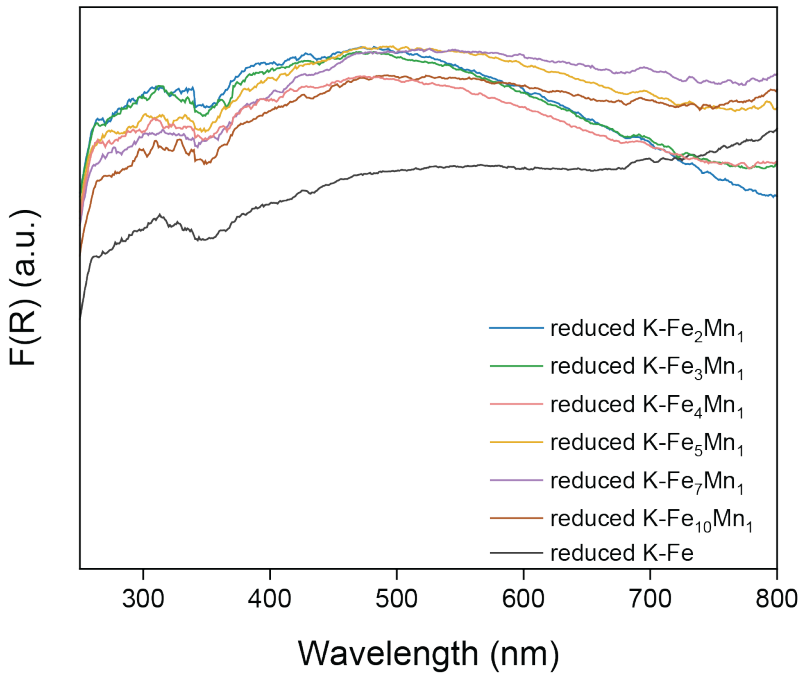

Figure S7. UV-vis-NIR absorption spectra of reduced K-Fe_xMn_y oxide.

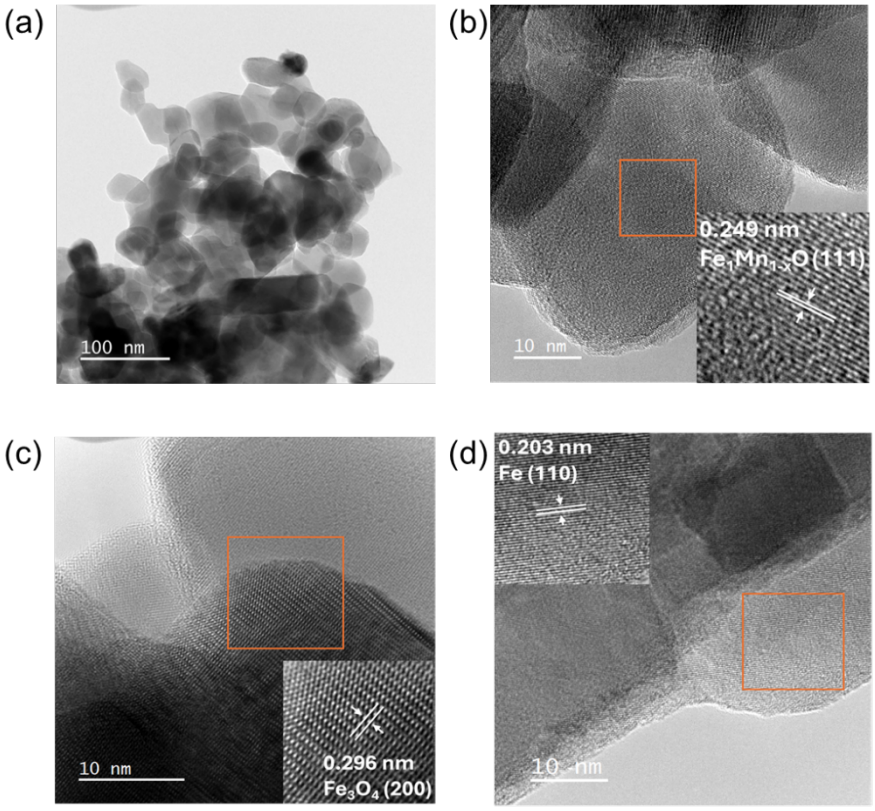

Figure S8. TEM images of the reduced K-$Fe_{10}Mn_1$ catalyst

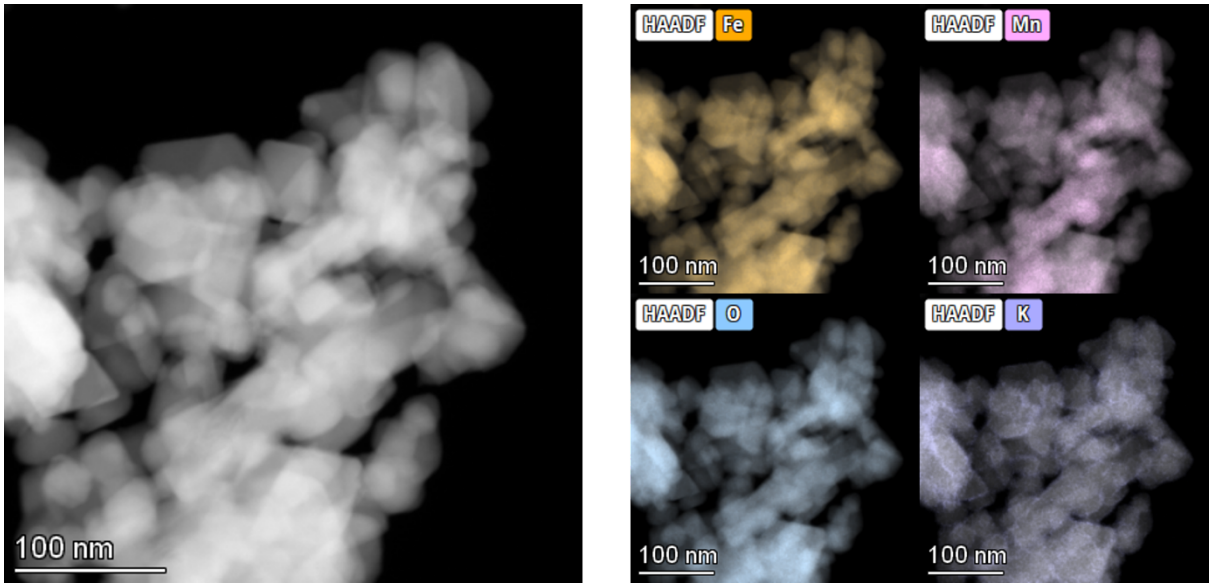

Figure S9. STEM images of reduced K-$Fe_{10}Mn_1$ catalyst with elemental mapping by EDX.

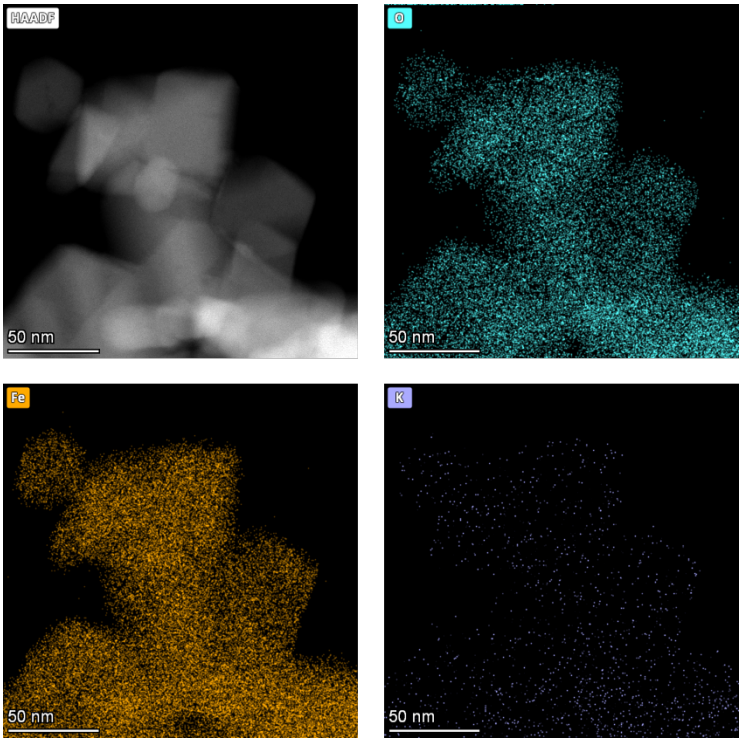

Figure S10. STEM images of the reduced monometallic K-Fe catalyst with elemental mapping by EDX.

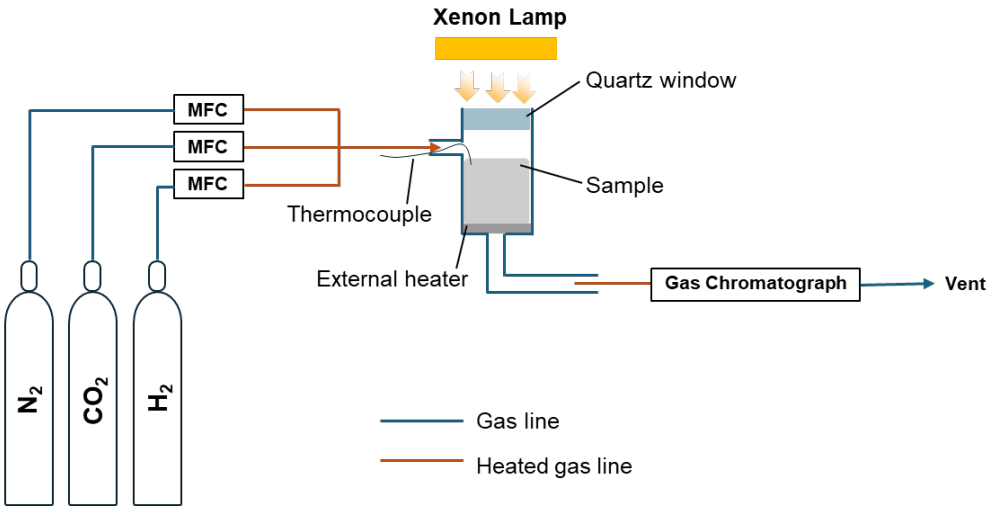

Figure S11. Schematic of the photothermal reactor setup.

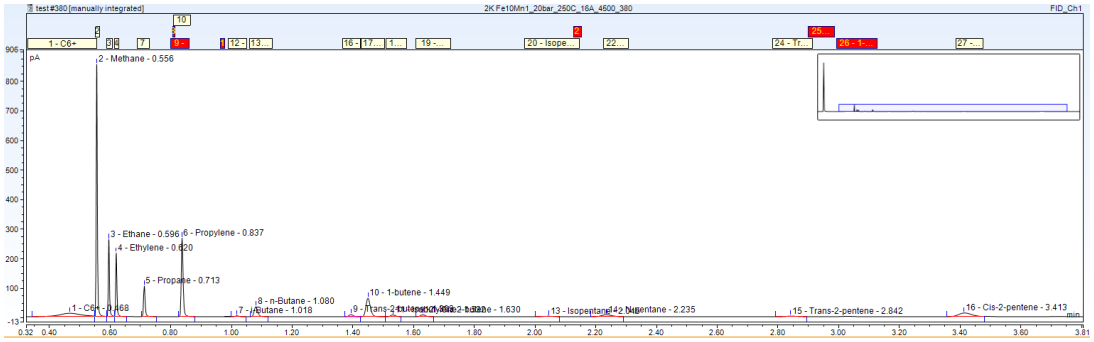

Figure S 12. The gas chromatograph profile over K-$Fe_{10}Mn_1$ catalyst under 4 W cm^{-2} light irradiation, 250 °C, 20 bar and 12000 mL g^{-1} h^{-1}.

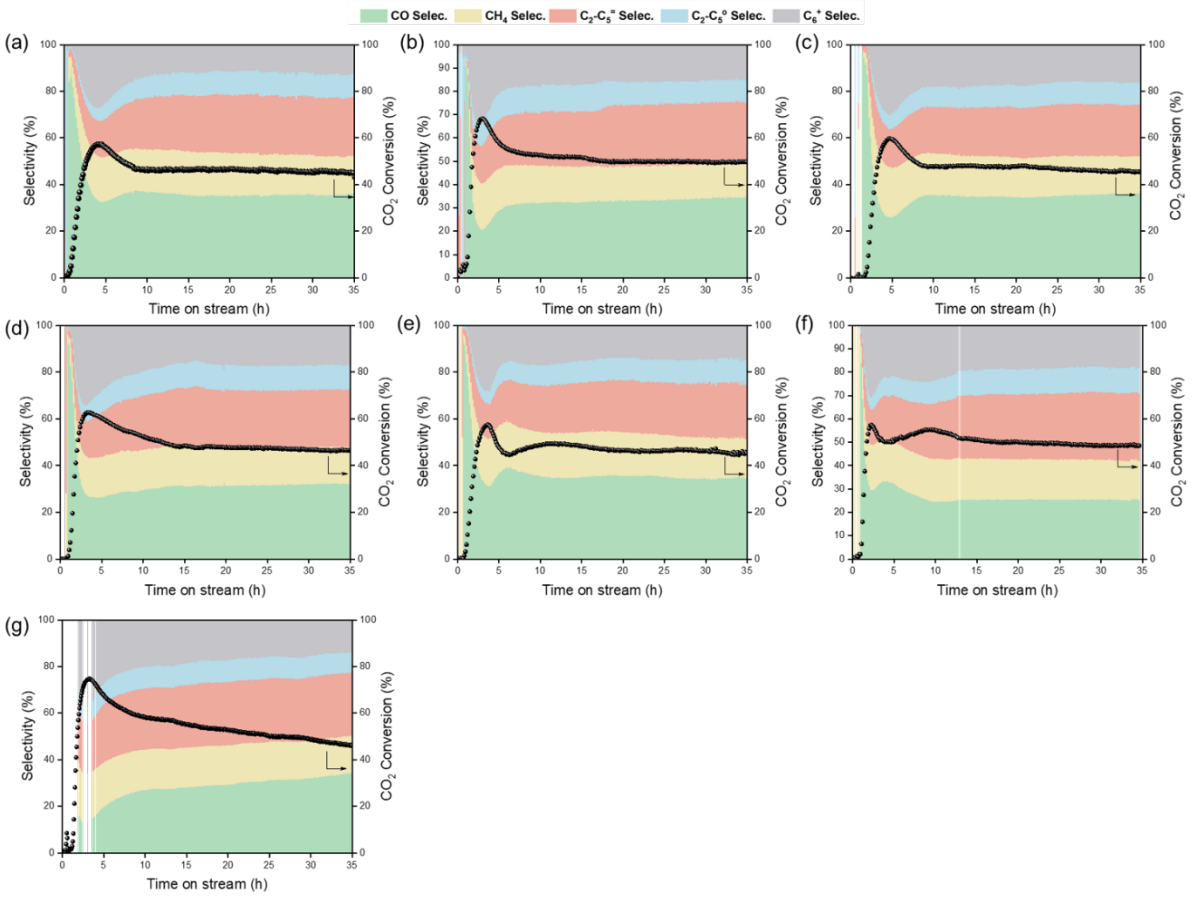

Figure S13. CO_2 conversion and product selectivity over (a) K-Fe_2Mn_1. (b) K-Fe_3Mn_1, (c) K-Fe_4Mn_1, (d) K-Fe_5Mn_1, (e) K-Fe_7Mn_1, (f) K-$Fe_{10}Mn_1$, and (g) K-Fe catalysts under 4 W cm^{-2} light irradiation with external heating at 250 °C at 20 bar. GSHV = 12000 mL g^{-1} h^{-1}, H_2/CO_2 =4.

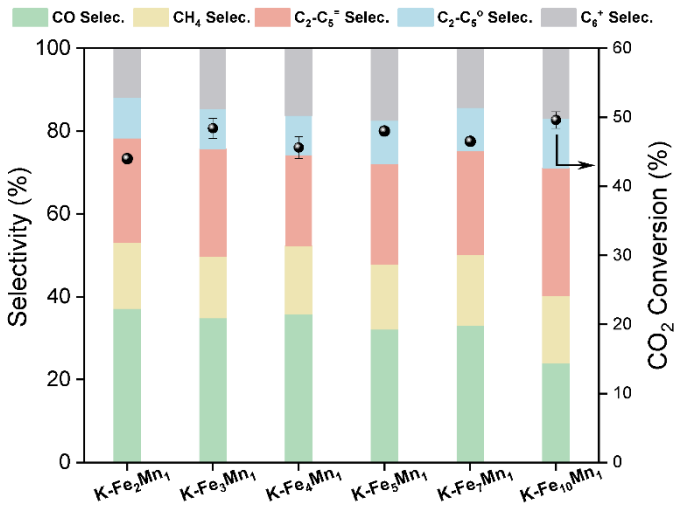

Figure S14. CO_2 conversion and product selectivity over K-Fe_xMn_y catalysts at TOS of 35 hours. Reaction condition: GSHV = 12000 mL g^{-1} h^{-1}, H_2/CO_2 =4, p = 20 bar, 4 W cm^{-2} light irradiation with external heating at 250 °C.

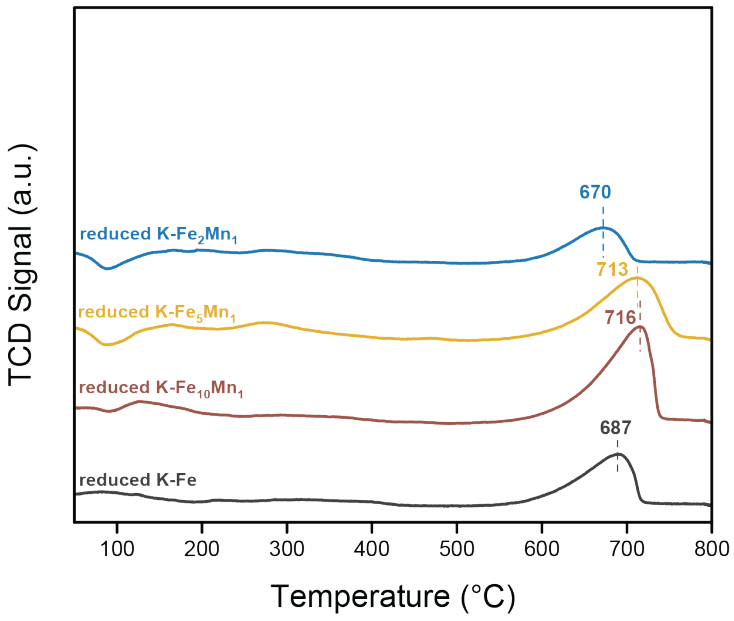

Figure S15. CO_2-TPD signal for reduced K-Fe_xMn_y/K-Fe samples.

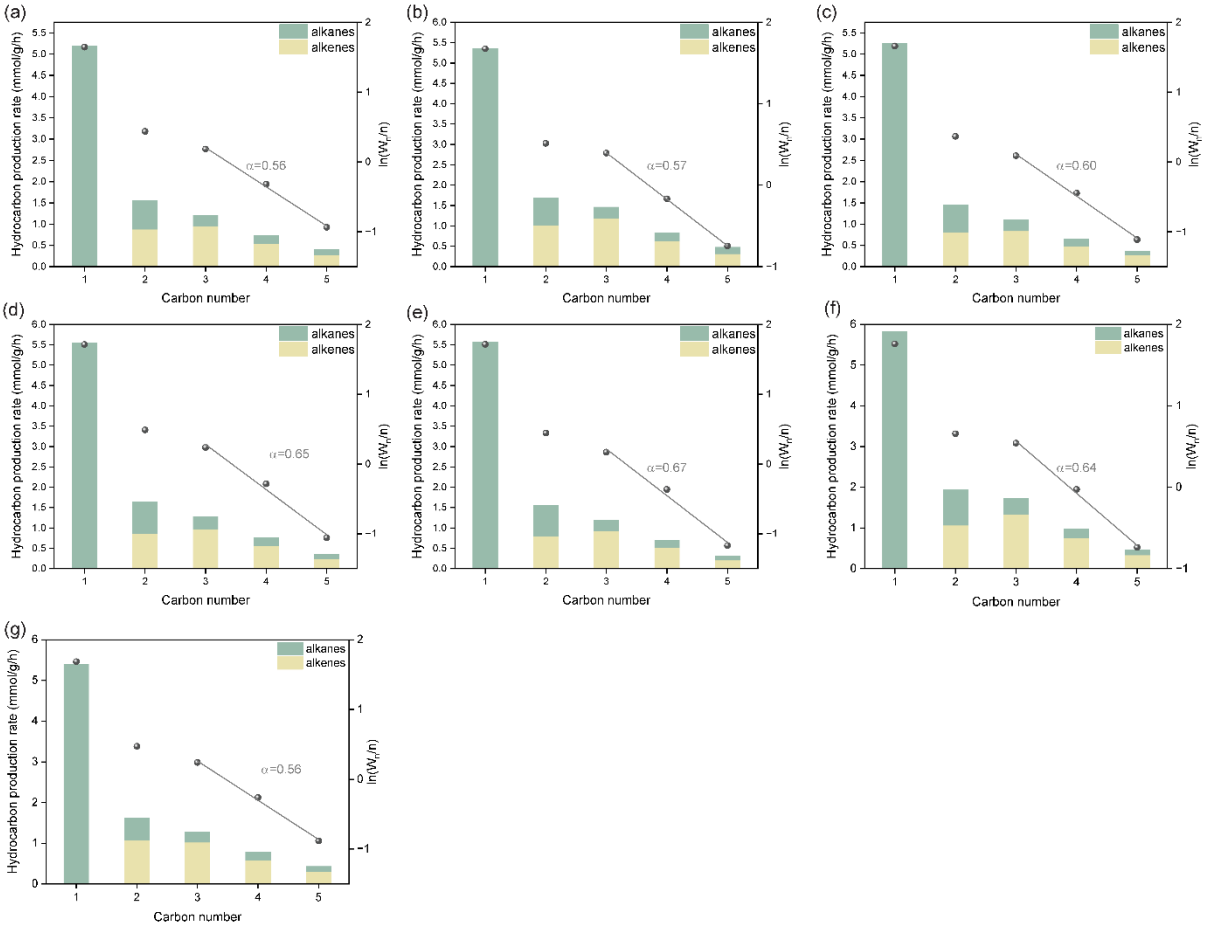

Figure S16. Hydrocarbon distribution and ASF plot on the (a) K-Fe_2Mn_1, (b) K-Fe_3Mn_1, (c) K-Fe_4Mn_1, (d) K-Fe_5Mn_1, (e)K-Fe_7Mn_1, (f) K-$Fe_{10}Mn_1$, and (g) K-Fe. Reaction conditions: 4 W cm^{-2} light irradiation with external heating at 250 °C, GSHV = 12000 mL g^{-1} h^{-1}, H_2/CO_2 =4, p = 20 bar, TOS = 35 hours.

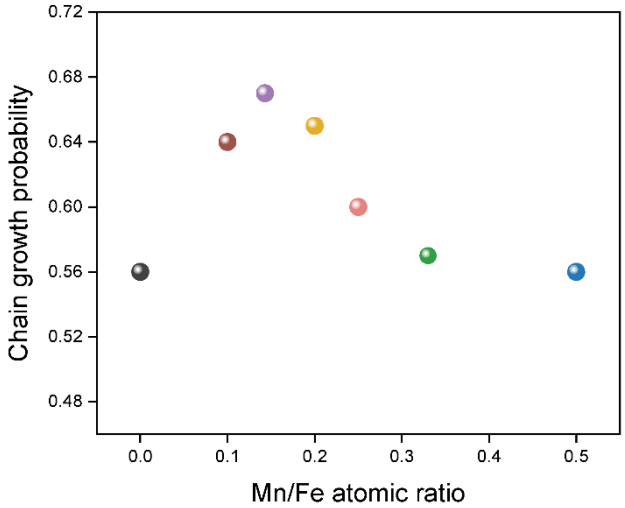

Figure S17. Chain growth probability as a function of Mn/Fe atomic ratio in K-Fe_xMn_y/K-Fe catalysts.

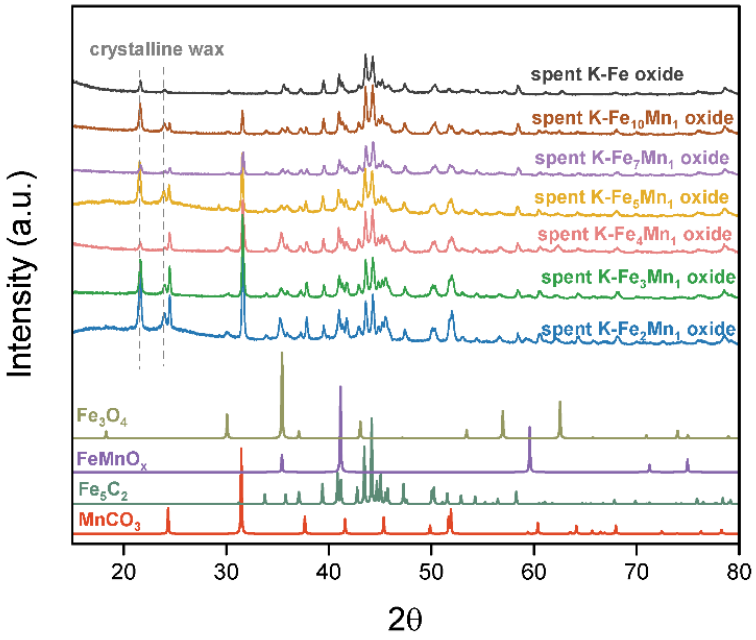

Figure S18. PXRD patterns for spent K-Fe_xMn_y/K-Fe catalysts after photo-thermal CO_2 hydrogenation reaction after TOS =35 hours at 20 bar under 4 W cm^{-2} irradiation with 250 °C external heating. Simulated XRD patterns for Fe_5C_2, Fe_3O_4, $Fe_1Mn_{1-x}O$, and $MnCO_3$ are included for reference.

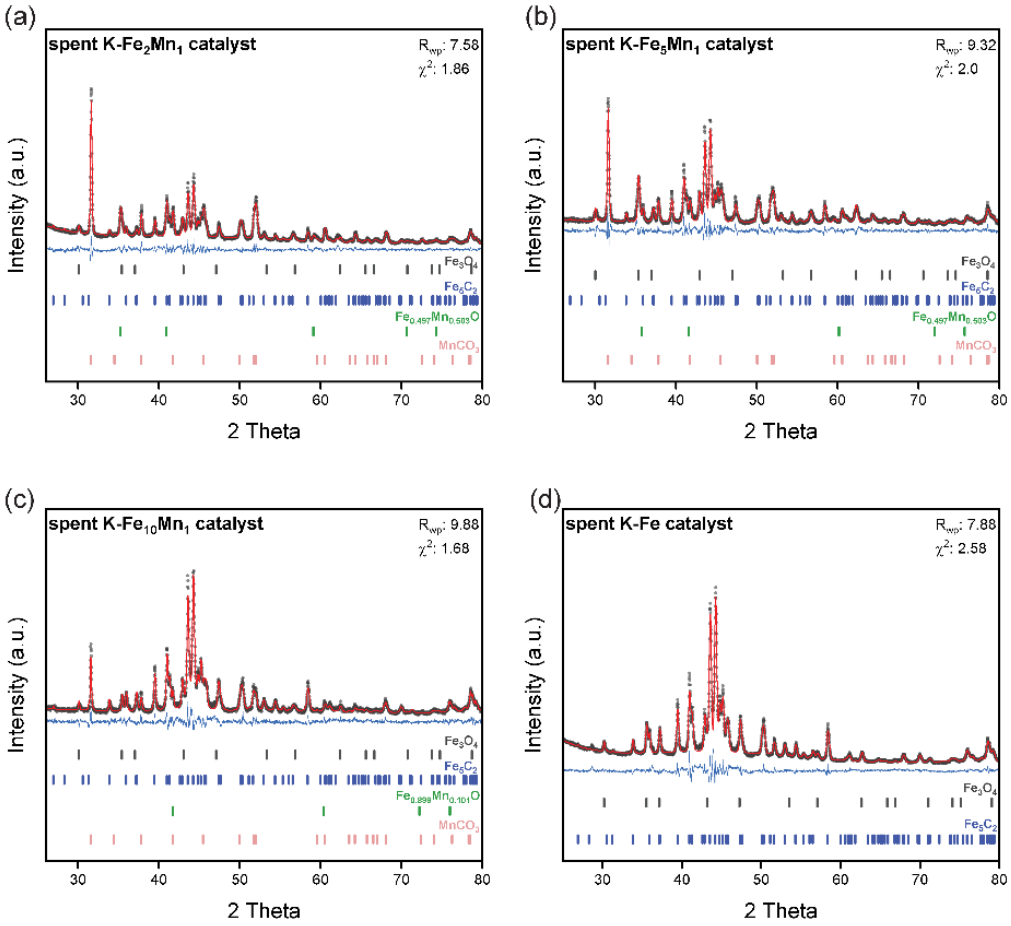

Figure S19. Rietveld plots showing obtained diffraction data, calculated intensities, and their difference for (a) spent K-Fe_2Mn_1, (b) spent K-Fe_5Mn_1, (c) spent K-$Fe_{10}Mn_1$, (d) spent K-Fe catalysts after photo-thermal CO_2 hydrogenation reaction after TOS =35 hours at 20 bar under 4 W cm^{-2} irradiation with 250 °C external heating.

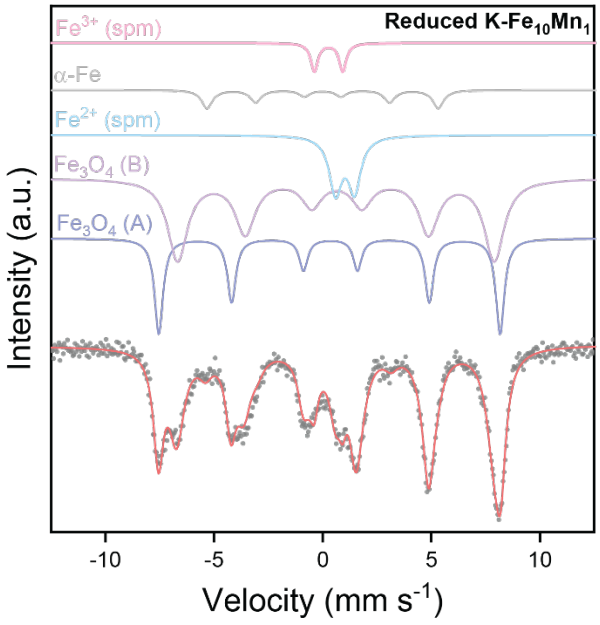

Figure S20. Mössbauer spectra of the reduced K-$Fe_{10}Mn_1$ catalyst.

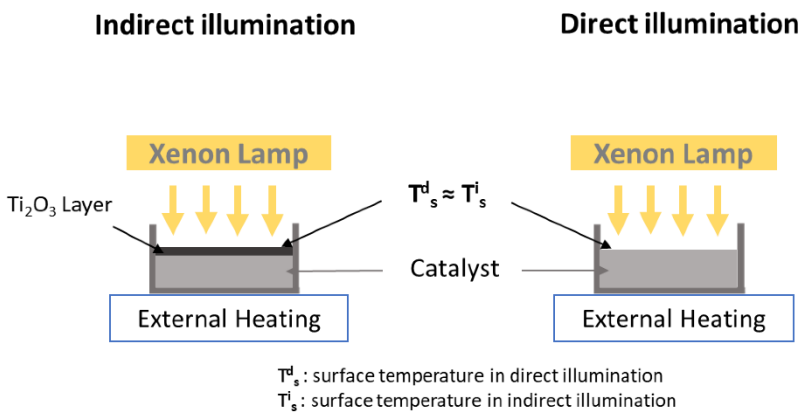

Figure S21. Illustration of direct and indirect illumination experiments.

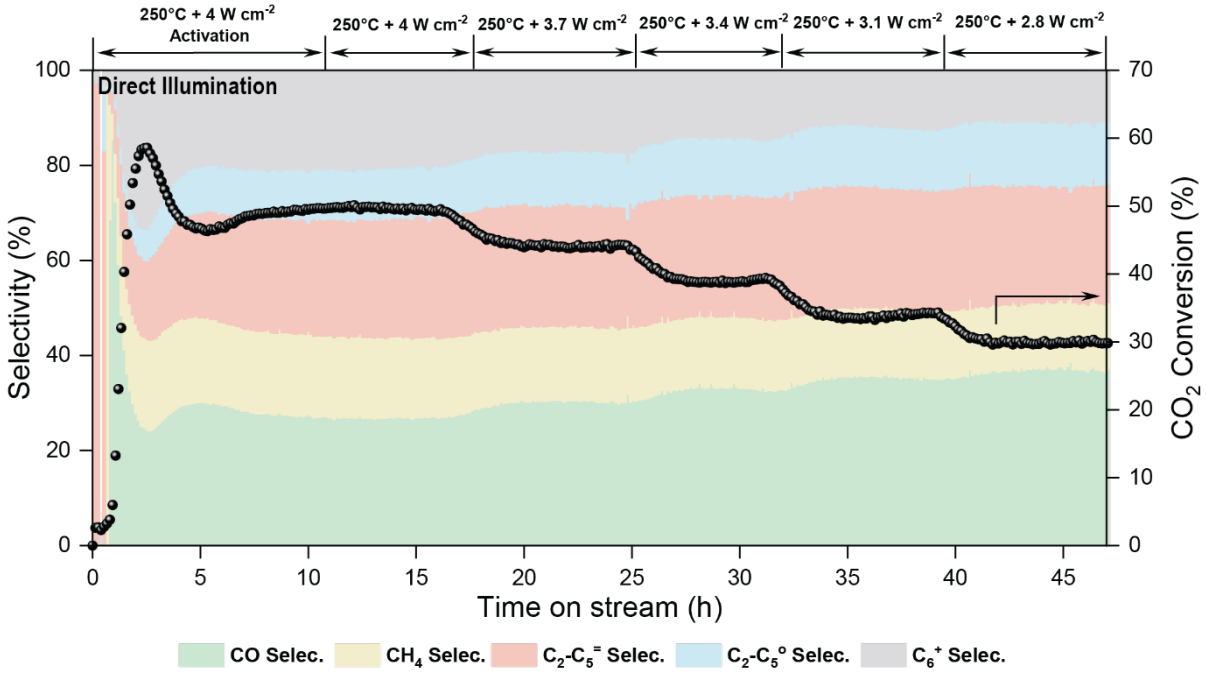

Figure S22. CO_2 conversion and product selectivity over K-$Fe_{10}Mn_1$ catalyst under direct 4 W cm^{-2} light irradiation with external heating at 250 °C at 20 bar. GSHV = 12000 mL g^{-1} h^{-1}, H_2/CO_2 =4.

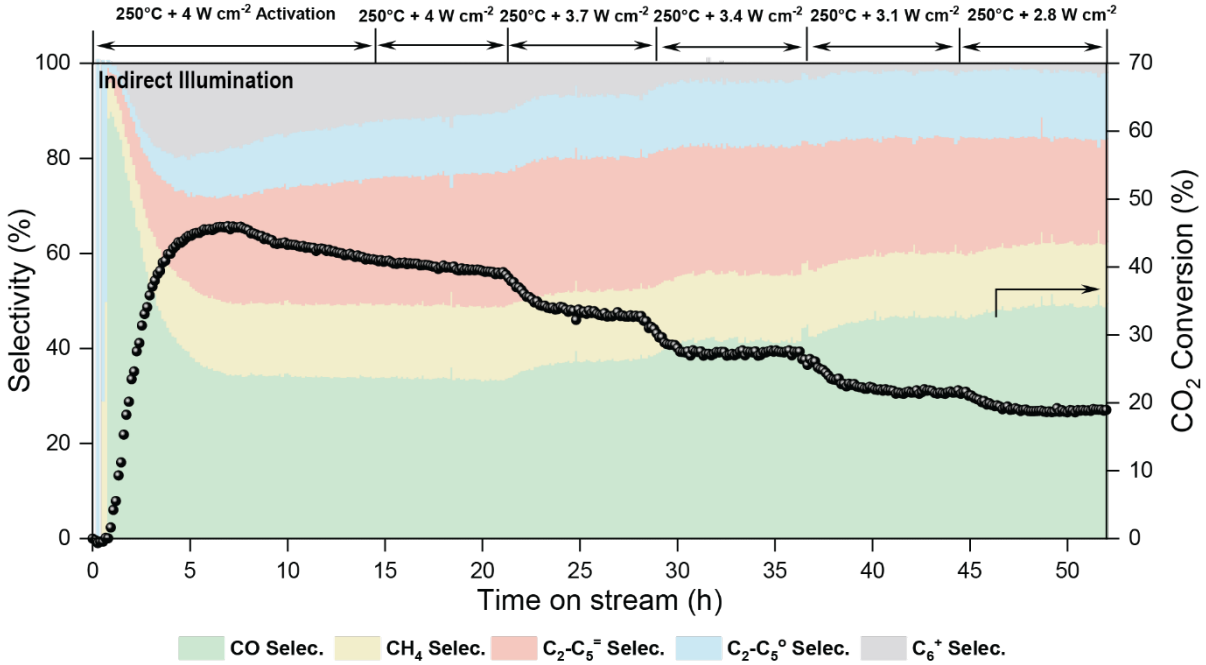

Figure S23. CO_2 conversion and product selectivity over K-$Fe_{10}Mn_1$ catalyst under indirect 4 W cm^{-2} light irradiation (cover with Ti_2O_3) with external heating at 250 °C at 20 bar. GSHV = 12000 mL g^{-1} h^{-1}, H_2/CO_2 =4.

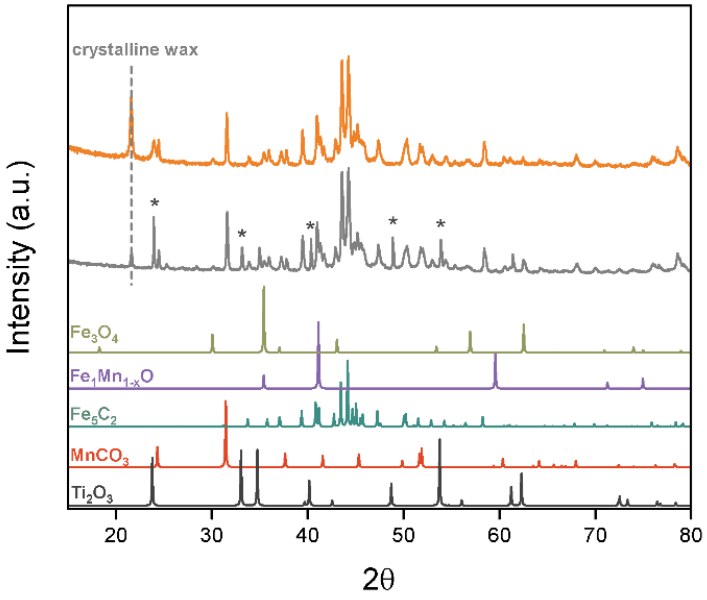

Figure S24. PXRD patterns for spent K-$Fe_{10}Mn_1$ catalysts after direct illumination (orange line) and indirect illumination (grey line) of 4 W cm^{-2} with 250 °C external heating. Reaction condition: GSHV = 12000 mL g^{-1} h^{-1}, H_2/CO_2 =4, p = 20 bar. Simulated XRD patterns for Fe_5C_2, Fe_3O_4, $Fe_1Mn_{1-x}O$, $MnCO_3$, and Ti_2O_3 are included for reference.

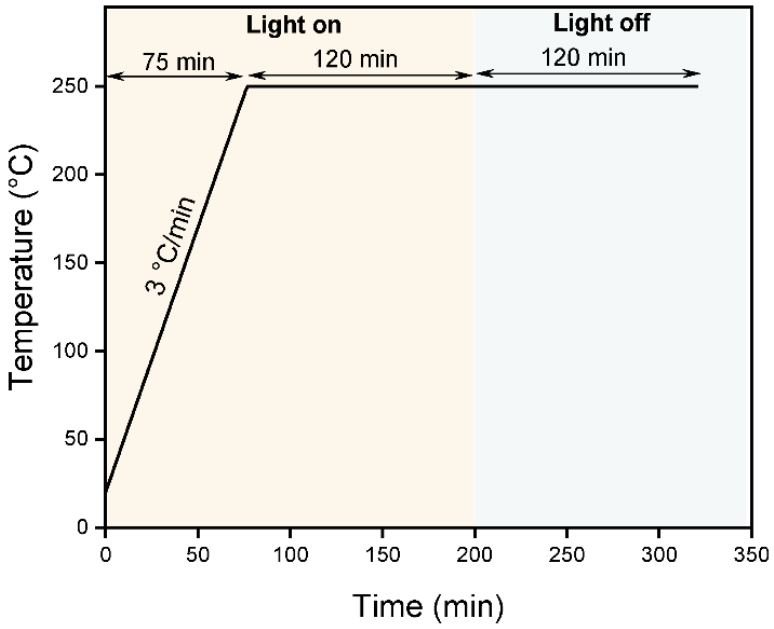

Figure S25. Experimental procedure of *in situ* DRIFTS measurement.

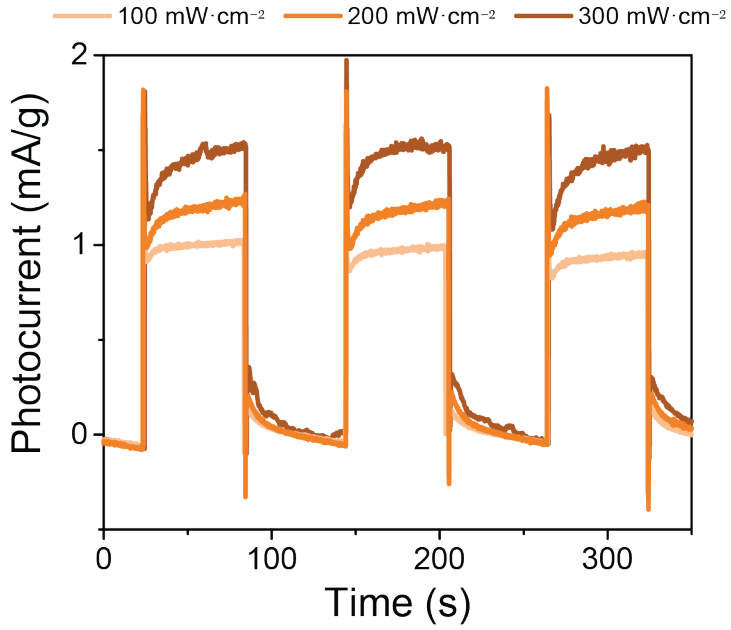

Figure S26. Transient photocurrent response under Xe lamp illumination (λ > 420 nm) of K-$Fe_{10}Mn_1$ at 300, 200, and 100 mW·cm^{-2} at 0.4 V vs Ag/AgCl.

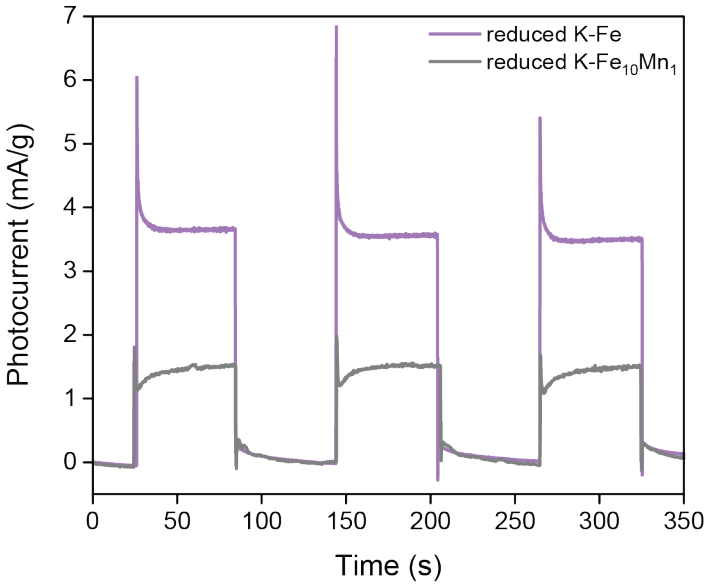

Figure S27. Transient photocurrent response under Xe lamp illumination (λ > 420 nm) of K-$Fe_{10}Mn_1$ and K-Fe at 0.4 V vs Ag/AgCl.

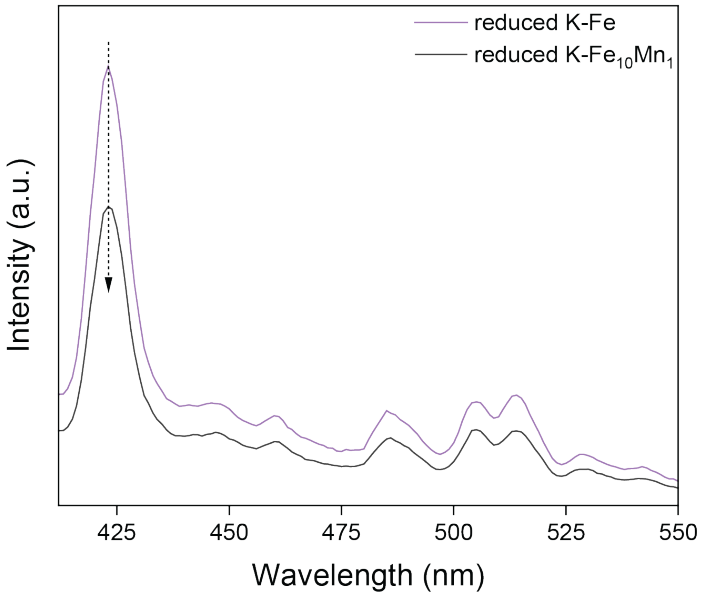

Figure S28. Steady-state photoluminescence (PL) analysis of K-Fe and K-$Fe_{10}Mn_1$ catalysts under 370 nm excitation.

3. Supplementary Tables

Table S1. X-ray fluorescence (XRF) analysis of the K-Fe_xMn_y samples.

Samples	Metal content (wt %)			Fe/Mn atomic ratio
	Fe (wt %)	Mn (wt %)	K (wt %)	
K-promoted $Fe_{10}Mn_1$	62.77	6.21	1.9	9.94
K-promoted Fe_7Mn_1	60.64	8.55	1.88	6.98
K-promoted Fe_5Mn_1	58.12	11.35	1.88	5.03
K-promoted Fe_4Mn_1	56.2	13.42	1.94	4.12
K-promoted Fe_3Mn_1	53.83	16.42	1.84	3.23
K-promoted Fe_2Mn_1	49.05	21.51	1.87	2.24

Table S2. Debye-Scherrer parameters of K-Fe_xMn_y/K-Fe samples.

Samples	2θ	Components	FWHM (radian)	Crystal Size (nm)*
K-promoted $Fe_{10}Mn_1$	35.73	α-Fe_2O_3	0.136	65.3
K-promoted Fe_7Mn_1	35.73		0.194	44.1
K-promoted Fe_5Mn_1	35.65		0.234	36.0
K-promoted Fe_4Mn_1	35.76		0.263	31.9
K-promoted Fe_3Mn_1	n.a.	-	n.a.	n.a.
K-promoted Fe_2Mn_1	n.a.	-	n.a.	n.a.

* The crystal size of α-Fe_2O_3 is estimated by the Debye-Scherrer equation.

Table S3. Specific surface area for K-Fe_xMn_y/K-Fe samples

Samples	Specific surface area
K-promoted Fe	26 $m^2 g^{-1}$
K-promoted $Fe_{10}Mn_1$	115 $m^2 g^{-1}$
K-promoted Fe_7Mn_1	287 $m^2 g^{-1}$
K-promoted Fe_5Mn_1	197 $m^2 g^{-1}$
K-promoted Fe_4Mn_1	197 $m^2 g^{-1}$
K-promoted Fe_3Mn_1	191 $m^2 g^{-1}$
K-promoted Fe_2Mn_1	172 $m^2 g^{-1}$

Table S4 Rietveld QPA (quantitative phase analysis)-based phase composition of reduced samples by analyzing their PXRD patterns in **Figure S6**.

Samples	Composition (wt%)		
	Fe_3O_4	$Fe_1Mn_{1-x}O$	α-Fe
Reduced K-Fe	95.5	-	4.5
Reduced K-$Fe_{10}Mn_1$	86.2	9.8	4
Reduced K-Fe_5Mn_1	77.2	20	2.8
Reduced K-Fe_2Mn_1	47.5	52.5	-

Table S5. Rietveld QPA (quantitative phase analysis)-based phase composition of spent samples by analyzing their PXRD patterns in **Figure S19**.

Samples	Composition (wt%)			
	Fe_5C_2	Fe_3O_4	$Fe_1Mn_{1-x}O$	$MnCO_3$
Spent K-Fe	91.0%	9%	-	-
Spent K-$Fe_{10}Mn_1$	84.1%	2.8%	2.1%	11%
Spent K-Fe_5Mn_1	56.7%	5.4%	5.2%	32.7%
Spent K-Fe_2Mn_1	43.0%	4.9%	10.6%	41.5%

Table S6. CO_2 conversion and products selectivity over K-Fe_xMn_y/K-Fe catalysts. Reaction conditions: 4 W cm^{-2} light illumination with 250 °C external heating at 20 bar, GSHV = 12000 mL g^{-1} h^{-1}

Samples	CO_2 Conv. (%)	Selectivity (%)			C_2^+ Selectivity (CO-free) (%)
		CO	CH_4	C_2^+	
K-$Fe_{10}Mn_1$	49.6	24.1	16.3	59.6	79.2
K-Fe_7Mn_1	46.5	33.2	17.1	49.7	73.4
K-Fe_5Mn_1	48.0	32.3	15.7	52.0	76.4
K-Fe_4Mn_1	45.6	36.0	16.2	47.8	75.1
K-Fe_3Mn_1	48.4	35.0	14.9	50.1	77.7
K-Fe_2Mn_1	44.0	37.3	15.9	46.8	74.6
K-Fe	45.7	34.4	16.1	49.5	75.2

Table S7. Mössbauer parameters for catalysts.

Samples	Iron species	IS (mm/s)	QS (mm/s)	H(T)	Species Contribution (%)
Reduced K-$Fe_{10}Mn_1$`	Fe_3O_4(A)	0.33	-0.02	48.82	38.60
	Fe_3O_4(B)	0.58	0.00	45.31	48.0
	Fe^{2+} (spm)	1.03	0.58	-	7.30
	α-Fe	0.00	-0.02	33.0	6.10
	Fe^{3+} (spm)	0.28	0.14	-	3.50
Spent K-$Fe_{10}Mn_1$	χ-Fe_5C_2 (I)	0.25	-0.04	21.89	35.80
	χ-Fe_5C_2 (II)	0.26	0.05	18.86	33.90
	χ-Fe_5C_2 (III)	0.19	0.05	10.32	22.90
	Fe_3O_4(A)	0.20	-0.26	49.08	2.30
	Fe_3O_4(B)	1.17	0.13	46.98	5.10
Spent K-Fe	χ-Fe_5C_2 (I)	0.26	-0.02	21.87	34.10
	χ-Fe_5C_2 (II)	0.19	0.04	18.78	33.90
	χ-Fe_5C_2 (III)	0.24	0.06	10.52	22.70
	Fe_3O_4(A)	0.18	0.27	48.42	3.10
	Fe_3O_4(B)	0.93	-0.04	46.40	6.20
Spent K-Fe_2Mn_1	χ-Fe_5C_2 (I)	0.26	0.02	21.95	31.30
	χ-Fe_5C_2 (II)	0.25	-0.03	19.25	29.60
	χ-Fe_5C_2 (III)	0.20	-0.02	10.90	18.90
	Fe^{2+} (spm)	1.05	1.30	-	4.60
	Fe_3O_4(A)	0.34	0.02	49.21	5.40
	Fe_3O_4(B)	0.64	-0.20	45.82	10.20

Table S8. Quantitative results of iron species over spent catalysts of XRD and Mössbauer measurements

Samples	Iron species	Composition (wt%)	
		Mössbauer	Rietveld QPA
Reduced K-$Fe_{10}Mn_1$	Fe_3O_4/Fe-containing oxide	93.9%	96.0%
	α-Fe	6.1%	4.0%
Spent K-$Fe_{10}Mn_1$	χ-Fe_5C_2	92.6%	94.5%
	Fe-containing oxide	7.4%	5.5%
Spent K-Fe	χ-Fe_5C_2	90.7%	91.0%
	Fe-containing oxide	9.3%	9.0%
Spent K-Fe_2Mn_1	χ-Fe_5C_2	79.8%	73.5%
	Fe-containing oxide	20.2%	26.5%

Table S9. CO_2 conversion of direct and indirect light illumination under different light intensities and over K-$Fe_{10}Mn_1$ catalyst. Reaction conditions: light illumination with 250 °C external heating at 20 bar, GSHV = 12000 mL g^{-1} h^{-1}

Light intensity (W·cm^{-2})	CO_2 conv. (%)[a]	CO_2 conv. (%) [b]	Difference of CO_2 Conversion Δ(%)
250 °C + 4W·cm^{-2}	49.6%	39.2%	20.96%
250 °C + 3.7 W·cm^{-2}	43.9%	32.7%	25.51%
250 °C + 3.4 W·cm^{-2}	38.8%	26.4%	31.96%
250 °C + 3.1 W·cm^{-2}	33.6%	21.5%	36.01%
250 °C + 2.8 W·cm^{-2}	29.8%	18.8%	36.9%

[a]: direct illumination; [b]: indirect illumination cover Ti_2O_3

Table S10. Performance comparison of different photothermal CO_2-to-hydrocarbon reactions.

Catalysts	H_2 : CO_2	Light source	P (bar)	T (°C)	Reactor type	GSHV (mL g^{-1} h^{-1})	CO_2 Conv. (%)	Selectivity (%)			C_2^+ Selec. in HC (%)	Productivity (mmol g^{-1} h^{-1})	Ref.
								CO	CH_4	C_{2+}			
Na-Co@C	5 : 1	1000 W Xe	2.8	235	Batch	-	37	50.2	4.8	36.3	44.9	-	3
$NiFe_9O_x$	5 : 1	1000 W Xe	0.27	-	Batch	-	94.5	2.8	59.5	40.5	40.5	-	4
CoFe Alloy/Al_2O_3	4 : 1	300 W Xe	1.8	320	Batch	-	78.6	4.97	59.77	35.26	37.1	-	5
Fe_3C	3 : 1	300 W Xe	1	310	Batch	-	-	9.2	81.2	9.6	10.6		6
MnO-Co	4 : 1	300 W Xe	1	150	Batch	-	10.2	trace	84.24	15.76	15.76	0.43 (C_{2+})	7
$CoFe_2O_4$	4 : 1	300 W Xe	1	300	flow	7900	12.9	50.0	20.2	29.8	59.6	1.1 (C_{2-4})	8
K-Ru/Fe_3O_4	3 : 1	300 W Xe	1	400	Batch	-	35	69.3	9.1	15.7	65.1	0.63 (olefin); 1 (C_{2+})	9
				420	flow	1500	-	-	-	-	-	0.25 (olefin)	
Co-Co_x/MAO	3 : 1	300 W Xe	3	325	flow	2400	23.7	35.2	24.3	40.5	62.5	1.3 (C_{2-4})	10
0.2KCFO	3:1	300 W Xe	3	305	batch	-	39.6	19.4	17.2	63.4	78.6	2.05 (C_{2-4})	11
			1	305	flow	3600	27	28.7	15.3	56.0	78.5	-	
K-$Fe_{10}Mn_1$	4 : 1	300 W Xe	20	250	flow	12000	49.6	24.1	16.3	59.6	79.2	4.8 (C_{2-5})	This work

Table S11. Performance comparison of different thermal CO_2-to-hydrocarbon reactions.

Catalysts	H_2 : CO_2	P (bar)	T (°C)	GSHV (mL g^{-1} h^{-1})	CO_2 Conv. (%)	Selectivity (%)			C_{2+} Selec. in HC (%)	Ref.
						CO	CH_4	C_{2+}		
FeMn0.1K0.1	3	20	320	20000	32.9	22.7	-	-	87.6	[12]
Fe/C-K_2CO_3	3	10	320	2400	32.4	21.4	-	-	87.3	[13]
Na-Zn-Fe	3	25	340	15000	39	14	-	-	88.6	[14]
9Fe-1Mn	3	15	350	3600	36.3	9.6	26.5	63.8	70.7	[15]
FeCo(0.1)/TiO_2	3	11	300	3600	33.3	6	51	43	45.7	[16]
Fe-Co/K-Al_2O_3	3	20	320	9000	38	25	14	61	81.3	[17]
Na–Fe_3O_4	3	30	320	8000	34	14	10	76	88.4	[18]
K-$Fe_{10}Mn_1$	4	20	250°C+4 W cm^{-2}	12000	49.6	24.1	16.3	59.6	79.2	This work

Reference

1. L. Finger, D. Cox and A. Jephcoat, *Applied Crystallography*, 1994, **27**, 892–900.
2. P. Thompson, D. Cox and J. Hastings, *Applied Crystallography*, 1987, **20**, 79–83.
3. L. Liu, A. V. Puga, J. Cored, P. Concepción, V. Pérez-Dieste, H. García and A. Corma, *Appl. Catal. B: Environ.*, 2018, **235**, 186–196.
4. A. V. Puga and A. Corma, *Topics in Catalysis*, 2018, **61**, 1810–1819.
5. G. Chen, R. Gao, Y. Zhao, Z. Li, G. I. Waterhouse, R. Shi, J. Zhao, M. Zhang, L. Shang and G. Sheng, *Adv. Mater.*, 2018, **30**, 1704663.
6. C. Song, X. Liu, M. Xu, D. Masi, Y. Wang, Y. Deng, M. Zhang, X. Qin, K. Feng and J. Yan, *ACS Catal.*, 2020, **10**, 10364–10374.
7. B. Zhao, M. Sun, F. Chen, W. Wang, S. Lu and B. Zhang, *ACS Catal.*, 2021, **11**, 10316–10323.
8. R. Song, Z. Li, J. Guo, P. N. Duchesne, C. Qiu, C. Mao, J. Jia, S. Tang, Y. F. Xu and W. Zhou, *Angew. Chem.*, 2023, **135**, e202304470.
9. C. Song, Z. Wang, J. Zhao, X. Qin, M. Peng, Z. Gao, M. Xu, Y. Xu, J. Yan and Y. Bi, *Chem Catalysis*, 2024, **4**.
10. S. Ning, H. Ou, Y. Li, C. Lv, S. Wang, D. Wang and J. Ye, *Angew. Chem. Int. Ed.*, 2023, **62**, e202302253.
11. S. Ning, X. Wu, H. Song, X. Ma, S. Yue, S. Zhang, L. Tang, R. Liu, X. Yin and S. Ouyang, *Journal of the American Chemical Society*, 2025.
12. H. Ren, H. Yang, J. Xin, C. Wu, H. Wang, J. Zhang, X. Bu, G. Yang, J. Li and Y. Sun, *Applied Catalysis B: Environment and Energy*, 2024, **358**, 124440.
13. Y. Han, C. Fang, X. Ji, J. Wei, Q. Ge and J. Sun, *ACS Catal.*, 2020, **10**, 12098–12108.
14. Z. Zhang, G. Huang, X. Tang, H. Yin, J. Kang, Q. Zhang and Y. Wang, *Fuel*, 2022, **309**, 122105.
15. Q. Yang, E. A. Fedorova, D.-B. Cao, E. Saraçi, V. A. Kondratenko, C. R. Kreyenschulte, H. Lund, S. Bartling, J. Weiß and D. E. Doronkin, *Nat. Catal.*, 2025, 1–12.
16. N. Boreriboon, X. Jiang, C. Song and P. Prasassarakich, *Journal of CO2 utilization*, 2018, **25**, 330–337.
17. C. C. Amoo, M. Li, A. Noreen, Y. Fu, E. Maturura, C. Du, R. Yang, X. Gao, C. Xing and N. Tsubaki, *ACS Applied Nano Materials*, 2020, **3**, 8096–8103.
18. K. W. Ting, T. Toyao, S. H. Siddiki and K.-i. Shimizu, *ACS Catal.*, 2019, **9**, 3685–3693.